

Subcritical transition to turbulence of a precessing flow in a cylindrical vessel

Johann Herault,^{1, a)} Thomas Gundrum,¹ Andre Giesecke,¹ and Frank Stefani¹
*Helmholtz-Zentrum Dresden-Rossendorf, P. O. Box 510119, D-01314 Dresden,
 Germany.*

(Dated: 22 September 2015)

The transition to turbulence in a precessing cylindrical vessel is experimentally investigated. Our measurements are performed for a nearly-resonant configuration with an initially laminar flow dominated by an inertial mode with azimuthal wave number $m = 1$ superimposed on a solid body rotation. By increasing the precession ratio, we observe a transition from the laminar to a non-linear regime, which then breakdowns to turbulence for larger precession ratio. Our measurements show that the transition to turbulence is subcritical, with a discontinuity of the wall-pressure and the power consumption at the threshold ϵ_{LT} . The turbulence is self-sustained below this threshold, describing a bifurcation diagram with a hysteresis. In this range of the control parameters, the turbulent flows can suddenly collapse after a finite duration, leading to a definitive relaminarization of the flow. The average lifetime $\langle \tau \rangle$ of the turbulence increases rapidly when ϵ tends to ϵ_{LT} .

^{a)}Electronic mail: j.herault@hzdr.de

I. INTRODUCTION

Rotating flows are ubiquitous in geophysical, astrophysical and industrial context. When an external torque is applied perpendicularly to the rotation axis of a solid body, it displays a precessing motion in order to conserve the angular momentum. The precession refers to the continuous change of direction of the axis of rotation, which rotates around the axis of precession. The response of a fluid flow driven by the precession of the vessel is a complex process¹, which results mostly in the interplay of inertial waves, Ekman boundary layers and base flow. It has been observed experimentally that the fluid flow driven by precession can amplify² a magnetic field, and simulations have demonstrated that a dynamo effect can operate^{3,4}. The present study belongs to the framework of the project DRESDYN⁵⁻⁷, which aims to investigate experimentally a precession driven dynamo.

The observed regimes and instabilities of a precessing flow depend strongly on the configuration, which includes the geometry (spherical, ellipsoidal or cylindrical), the rotation of the body, and the strength of the precession. For sake of clarity, we recall only the results in cylindrical geometry. In most of the experimental investigation, the set-up is composed of a cylinder rotating around its revolution axis at the rotation rate Ω_c and this cylinder is mounted on a turntable rotating at the precession rate Ω_t . When the angle between the axes of rotation and precession is non-zero, the flow deviates from the solid body rotation, due to the acceleration of the rotation axis. Initially observed by McEwan⁸, the laminar flow is composed of Kelvin modes superimposed on a solid body rotation⁹⁻¹². The Kelvin modes¹³ (or inertial modes) are the eigen-modes of a rotating cylindrical vessel. Each mode has its own eigen-frequency ω , which depends on the radial, axial and azimuthal wave numbers. The gyroscopic force due to the precession excites the modes with azimuthal wave number $m = 1$ and angular frequency Ω_c . A mode can be resonant if its eigen-frequency is close to the angular forcing frequency Ω_c . Out of the resonance, the amplitude of the modes scales like $|\omega - \Omega_c|^{-1}$ and it increases with the strength of the precession, quantified by the precession ratio $\epsilon = \Omega_t/\Omega_c$. At the resonance, viscous and non-linear effects play an important role in the saturation of the amplitude of the Kelvin modes^{10,11,14,15}.

Suggested by McEwan⁸, Kerswell¹⁶ has demonstrated that the Kelvin modes forced by precession become unstable by a parametric instability. The mechanism is based on a triadic resonance with two other free Kelvin modes, i.e. two modes not directly forced by

the precession. Lagrange *et al.*^{17,18} confirmed experimentally this scenario for a precessing flow with a single forced Kelvin mode close to its resonance. The parametric instability can either saturate¹⁸ or trigger a secondary instability called resonant collapse^{8,19,20}. A weakly non-linear analysis performed by Lagrange *et al.*¹⁸ predicts a subcritical bifurcation leading to a stationary state or a cyclic dynamics for larger Reynolds number. When the instability does not saturate, a sequence of bifurcations called resonant collapse triggers a breakdown of the flow into a small-scale chaotic flow. Manasseh¹⁹ pointed out that the most violent resonant collapse occurs for the resonant Kelvin mode with the smallest radial wave number (called type *A* breakdown), leading to a fine-scale turbulence. The resonant collapse can display a cyclic dynamics with a transient chaotic phase followed by a relaminarization of the flow^{8,20}. During the chaotic phase, the kinetic energy remains mostly in modes with frequencies in the range of those of the inertial modes²⁰.

It is tempting to speculate that the turbulence appears progressively from the chaotic set associated with the resonant collapse, but the experimental observations reports a more complex road to turbulence. Indeed, by further increasing the precession ratio, Lin *et al.*²⁰ observed a non-linear regime after the resonant collapse, characterized by the disappearance of the free Kelvin modes in the power-spectrum. At critical precession ratio, a sustained intense turbulent flow fills the vessel^{21,22}. Gans²² reported a discontinuity of the torque curve at the transition to turbulence. The torque curves exhibits also a hysteresis between the turbulent and non-turbulent branches. A similar bistability has been reported by Mouhali *et al.*²¹ in a cylinder and by Malkus² in a ellipsoidal geometry. The presence of a discontinuity and the hysteresis suggests that a subcritical instability triggers the turbulence for these experiments with large Reynolds number ($Re > 10^5$). The nature of the transition to turbulence remains unclear.

In the framework of dynamical systems, the so-called subcriticality refers to a transition from a base state to a new state (here turbulent), such that the new state is created from one or a sequence of bifurcations²³, which does not change the local stability of the base state. It is analogue to a first-order phase transition, like the vapour-liquid transition of water below the critical point. The transition is generally abrupt and violent and the triggering depends on the strength of the perturbation if the flow remains linearly stable. In the past fifty years, great progress has been made to understand the subcritical bifurcation to turbulence in shear flows, like pipe flows²⁴ or Plane-Couette flows^{25–27}. Recently, those concepts have

been extended to magnetohydrodynamics flows^{28–30}. Subcritical bifurcation in shear flows is characterized by specific properties^{24,31}, such as non-normal growth, complex structures of the flow pattern and finite lifetimes of the turbulence^{32–36}.

The finite lifetime of the turbulence is one of the most striking features of shear flows undergoing a subcritical bifurcation to turbulence. The perturbations leading to turbulent spots may relaminarize after a finite duration. The lifetimes of turbulence are random and their mean value increases rapidly with the Reynolds numbers. It turns out that the turbulence is a metastable regime for a range of Reynolds numbers. This feature has been observed in hydrodynamic shear flows (pipe flow³², Plane-Couette flow³³ or stable Taylor-Couette flow³⁴) and in magnetohydrodynamics shear-flows^{35,36}.

In the present study, we investigate the subcritical transition to turbulence in a fluid flow driven by a precessing cylindrical vessel. The observed transition to turbulence is a robust process and occurs above a well defined threshold different from the threshold of the parametric instability of the forced Kelvin mode. Below the threshold of the subcritical transition, the turbulence is self-sustained, describing an hysteresis bifurcation diagram. We show that the turbulence is metastable in the hysteresis region and can cease suddenly.

Section II introduces the experimental set-up and the dimensionless control parameters. In section III, the regimes appearing before the turbulence are briefly reviewed. The quantitative features of the turbulence and the associated subcritical bifurcation are presented in section IV. Section V presents the experimental investigation of the finite lifetime of the turbulence.

II. THE EXPERIMENTAL DEVICE

A. Experimental setup

The experimental setup is illustrated on the Fig. 1. The vessel is a cylinder of radius $R = 163$ mm and height $h = 326$ mm. It is completely filled with water. For the visualization of the flow (see Fig.2), a small amount of air is introduced. The bubbles are only used to visualize the flow pattern and all the quantitative results have been obtained with a very small amount of bubbles. The container rotates around its symmetry axis. The cylinder is driven by an asynchronous 3 kW motor via a transmission chain. The power is supplied by a

slip ring. To improve the parallelism of the end caps of the cylinder, they are joined together by eight rods (yellow rods on the right Fig.1). The end-cap located at the opposite side of the motor is maintained by a counter bearing, in order to avoid any bending. This structure is mounted on the turntable. It can be tilted to vary the inclination between the direction of the rotation of the cylinder and the direction of the precession. In the present study, the angle is constant at 90° so that rotation axis and precession axis are orthogonal like in refs^{20,21}. The turntable is driven by a second asynchronous 2.2 kW motor. The frequency rate of the turntable f_t can be increased up to 1Hz. We have not used a control loop for the motors, in order to avoid perturbations due to the control process, like self excitations, which stress the mechanics of the experiment. The rotation rates of the cylinder and the turntable are continuously measured by two tachometers. The fluctuations of the rotation rates are smaller than 0.05% and the rotation rates do not vary during the transitions from and to the turbulent regime.

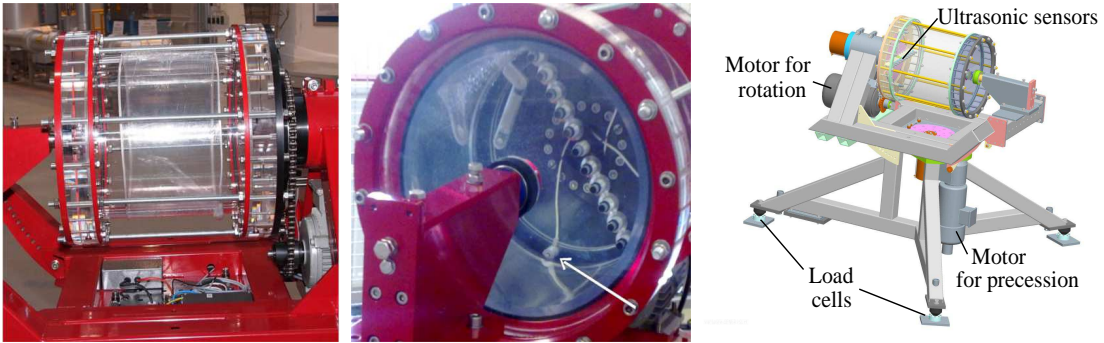


FIG. 1. Left: photography of the precessing cylinder. Center: transversal photography. The white pressure sensor is located at the bottom of the end-cap, close to the lateral-wall (white arrow). An array of UDV sensors is also visible. Right : sketch of the experiment.

B. Measurement techniques

1. *Power consumption measurement*

The power consumption of the three-phase asynchronous motors is calculated by measuring the input current on a single phase and the voltage difference between two phases. Here, we report only the power consumption of the motor of the cylinder. The measurement of the

current is performed with a Tektronix current-clamp TCP312 and amplified by a TCPA300 amplifier with a typical accuracy of 1%. The voltage is measured by a differential probe Sapphire SI-9010. The amplitudes of the current $I(t)$, the amplitude of the voltage difference $U(t)$ and their relative phase $\phi(t)$ are extracted by a Hilbert transform. The internal resistance of the motor R_I has been measured by a 4 wires technique after a long run, in order to measure R_I close to the operating conditions (effect of the internal heating). The functions $U(t)$, $I(t)$ and $\phi(t)$ vary on time scales much larger than the rotation period of the motor. The instantaneous power consumption $P(t)$ of an equilibrated motor is defined by

$$P(t) = \frac{\sqrt{3}}{2} U(t) I(t) \cos \left(\phi(t) + \frac{\pi}{6} \right) - \frac{3}{4} R_I I(t)^2. \quad (1)$$

Because $I(t)$ and $U(t)$ are the peak values, the product UI and I^2 must be multiplied by the factor $1/2$ to obtain the RMS values. The relative phase $\phi(t)$ has been shifted by $\pi/6$ in order to obtain the relative phase between the current and the voltage for the same phase. The average power consumption is given by $P_m = T^{-1} \int_0^T P dt$, with T the duration of the measurement. The value P_m can be decomposed into the sum of the mechanical loss, the magnetic loss and the power dissipated by the flow. Only the latter is of interest to us. We expect that the magnetic and mechanical losses do not change significantly for constant rotation rate Ω_c . Their values have been measured for runs at $\Omega_t = 0$ (no precession), which corresponds to a solid body rotation without power dissipated by the flow. Our measurements show that the power consumption increases like Ω_c^2 for $\Omega_t = 0$.

2. *Pressure measurement*

The pressure is measured at the end-cap close to the motor (see center Fig.1). Two XPM5 miniature pressure sensors are mounted flush on the rotating end-cap. They are on the same radius with respect to the axis of revolution, located at $r = 160$ mm. Their diameter is 3.6 mm. In the present study, we focus only on the pressure variation. In section III, we present the frequency power spectrum. The power spectra are rescaled in order to have a power spectral density $PSD[p](f)$ tending to 1 for low frequencies. In the rest of the paper (section V and IV), we have used a smoothing filter to low-pass filter the signal with a typical cut-off frequency $f_c/2$. The purpose of the filter is to suppress the components with frequencies equal or larger than the frequency rate of the cylinder f_c in order to diagnose the variation

of the slow components.

C. Dimensionless number

We recall all the parameters characterizing our set-up in the table I.

Parameters	Definition	Value
ν	Kinematic viscosity	$10^{-6} \text{m}^2 \text{s}^{-1}$
R	Radius	163 mm
h	height	326 mm
$f_c = \Omega_c/2\pi$	Rotation frequency	0 – 10Hz
$f_t = \Omega_t/2\pi$	Precession frequency	0 – 1Hz
Θ	Precession angle	90°

TABLE I. Physical parameters of the experimental setup.

The dimensional analysis allows us to define three dimensionless numbers from the five parameters $(h, R, \nu, \Omega_c, \Omega_t)$ (we consider Θ as a dimensionless number)

$$\Gamma = \frac{h}{2R}, \quad \epsilon = \frac{\Omega_t}{\Omega_c}, \quad Re = \frac{\Omega_c R^2}{\nu} \quad (2)$$

Γ is the aspect ratio and is equal to 1. It plays an important role in the determination of the eigen-frequency of the Kelvin modes³⁷. The Reynolds numbers Re quantifies the dissipative process and can be varied in the range $[1.6 - 16.5] \times 10^5$. The effects of the precession are quantified by the precession ratio ϵ , which varies in the range 0 – 0.16. Only the latter two dimensionless numbers can be modified. In the present study, the Reynolds number is only changed for studying the scaling of the power dissipated at constant ϵ (section IV A) and the parameter space (section IV C). In the most part of the paper, the Reynolds number is fixed to $Re = 5.65 \times 10^5$.

III. THE FLOW REGIMES

Before focusing on the transition to turbulence, we present the different regimes observed in the precessing experiment. We distinguish three regimes by increasing progressively the

precession ratio ϵ for a constant Reynolds number Re , thanks to a direct visualization of the flows (see Fig.2) or by analysing the power spectrum of the pressure signal (see Fig.3). Visualization and pressure measurements have been performed for two different Reynolds numbers: $Re = 14 \times 10^5$ for the visualization and $Re = 5.65 \times 10^5$ for the pressure measurements.

Our classification holds for the range $Re \in [1, 14] \times 10^5$ and the parametric study of the regimes is reported in the section IV C (cf Fig. 7). The three regimes are

1. the laminar regime,
2. the non-linear regime,
3. the turbulent regime.

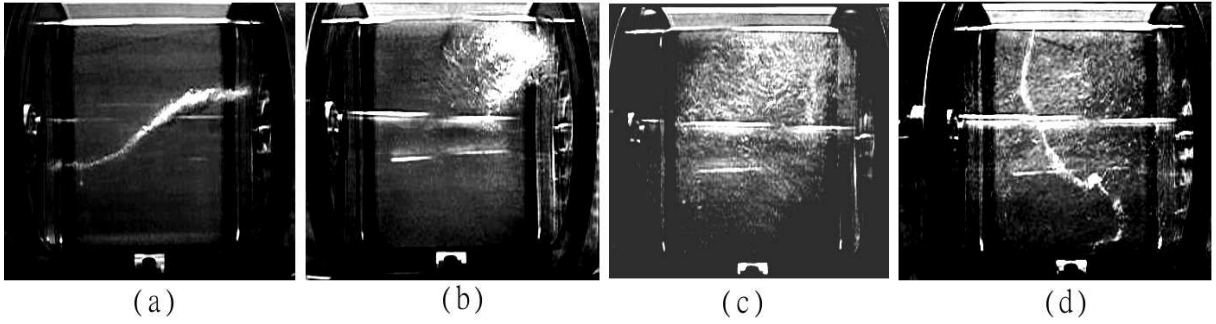


FIG. 2. The different regimes of the precessing flow are observable, via a small amount of bubbles, in the precessing reference frame (turntable frame) for $f_c = 10Hz$ and $\epsilon = 0.74 \times 10^{-2}$ (a), 5.9×10^{-2} (b), 7.4×10^{-2} (c), and 10×10^{-2} (d). The amount of air is kept constant. From left to right : standing forced Kelvin mode with a S-shape (a), non-linear regime with almost not distinguishable Kelvin modes and the bubbles localized in the upper left region (b), turbulent regime with an important spreading of the bubbles (c), strong vortex superimposed with turbulent fluctuations (d).

The laminar flow corresponds to a superposition of Kelvin modes with an azimuthal wave number $m = 1$. Following the theory of precessing flow³⁷, the first resonance occurs at $f = 0.996f_c$ for an aspect ratio $h = 1$. Our configuration corresponds to a resonant case with one dominant Kelvin mode. In the Fig. 2(a), we clearly identify the S-shape of the

minimal pressure region, associated with the axial wave number $k_z = \pi \cdot L^{-1}$. It is standing in the turntable frame. The power spectrum of the pressure signal exhibits an intense peak at the frequency f_c and at the corresponding harmonics (see Fig.3(a)). The peaks at $2f_c$ and $3f_c$ likely arise from non-linear self-interaction of the forced Kelvin mode¹¹. For a forced Kelvin mode defined by the frequency f_c , an azimuthal wave number $m = 1$ and an axial wave number k_0 , the non-linear interaction will drive the modes $(2f_c, m = 2, k = 0)$ and $(0, 0, k = 2k_0)$ (the other combinations are forbidden). Moreover, the inertial pressure term, given by $|\Omega \times \vec{r}|^2$, contributes to the component $f = 2f_c$ ¹¹. The centrifugal pressure and the hydrostatic pressure contribute also to the pressure components at f_c .

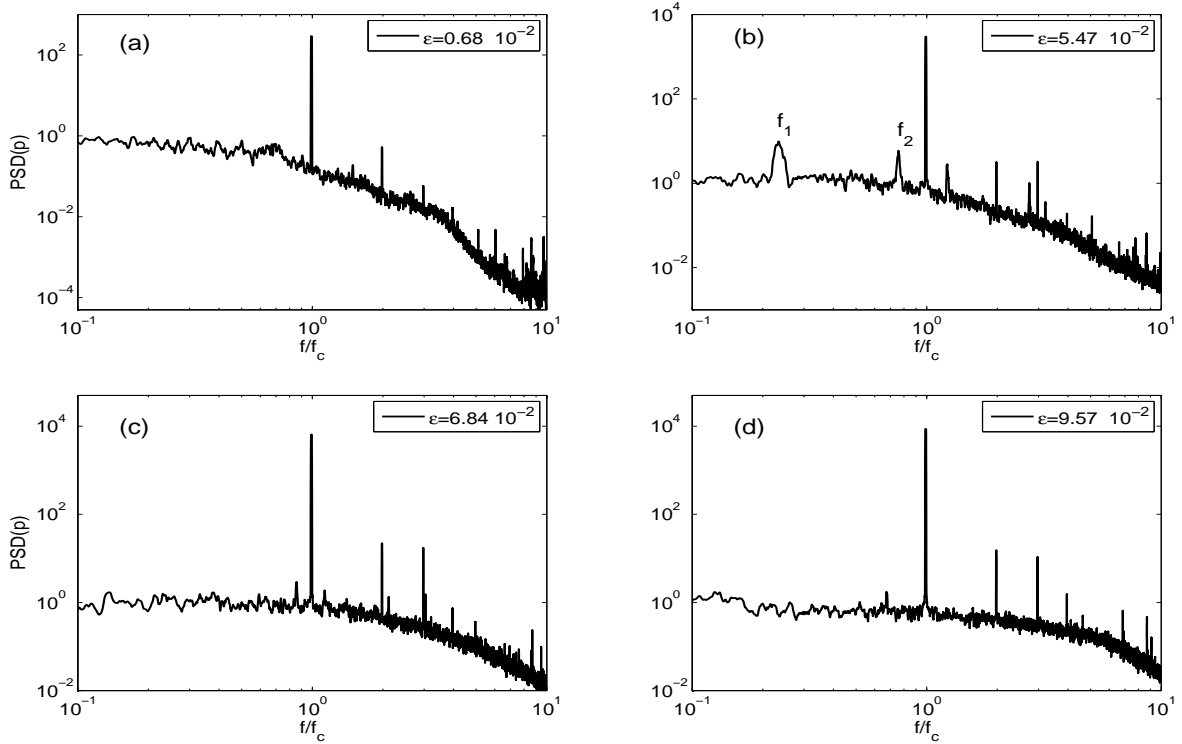


FIG. 3. Power spectrum of the pressure signal for $Re = 5.65 \times 10^5$ and $\epsilon = 0.68 \times 10^{-2}$ (a) (laminar regime), $\epsilon = 5.47 \times 10^{-2}$ (b) (non-linear regime with triadic resonance), $\epsilon = 6.84 \times 10^{-2}$ (c) (non-linear regime without triadic resonance) and $\epsilon = 9.57 \times 10^{-2}$ (d)(turbulent regime).

We define as non-linear regime the regime between the first instability of the Kelvin mode $m = 1$ and the transition to turbulence. At a given precessing ratio, the forced Kelvin mode becomes unstable. Indeed, the peaks observed on the power spectrum (see Fig.3(b)) suggest the existence of two free Kelvin modes ($f_1 = 0.223f_c$ and $f_2 = 0.75f_c$) in near-resonance

with the forced Kelvin mode ($f_1 + f_2 = 0.97f_c$). The thresholds of appearance of these triads will be discussed later (Fig. 7). At the threshold, the peaks in the power-spectrum correspond to frequencies close to $f_1 = 0.35f_c$ and $f_2 = 0.65f_c$, which may be assigned to $m = 5$ and $m = 6$ modes. By further increase of the precession ratio, these frequencies vary. We believe that this effect is due to the saturation process which is achieved by a detuning in frequency of the modes (see for instance¹⁸). These results will be reported in a future paper.

Further increasing the precession ratio, we have identified a sequence of bifurcations, and we are currently designing a velocimetry set-up to diagnose in details these bifurcations. These results will be reported in a future paper. For larger precession ratio, the two previous frequency peaks disappear (see Fig.3(c)) and the power-spectrum becomes flatter. The forced Kelvin mode is no more distinguishable by direct visualization (see Fig.2(b)). The bubbles are localized close to one end-cap due to the breaking of the centro-symmetry of the laminar flow.

These observations suggest that the dynamics is already complex and likely chaotic. Our measurements are consistent with the observations of Lin *et al*²⁰, who observed the disappearance of triadic resonance of inertial modes in the strongly non-linear regime.

Further increasing the precession ratio, the flow becomes turbulent. The properties of this transition will be detailed in the following sections. Visually, the turbulent flow is characterized by the spreading of small bubbles in the full vessel (see Fig.2(c)). Occasionally, we observe a vortex filament aligned with the direction of precession (see Fig.2(d)). The pressure signal gives few information about the turbulent flow (see Fig. 3(d)). The power-spectrum becomes almost flat on the range of frequencies $f < 4f_c$.

IV. TURBULENCE AND SUBCRITICAL BIFURCATION

In this section, we focus on the transition to turbulence. First, we confirm the existence of a discontinuity and a hysteresis of the power consumption at the transition²². Then, we study the dynamics and the robustness of this transition. We conclude this section by the systematic determination of the threshold in function of the Reynolds number.

A. Power consumption: hysteresis and scaling

We carried out measurements of power consumption at constant Reynolds number $Re = 5.65 \times 10^5$ ($f_c = 4\text{Hz}$). We have performed a first ascending series of measurements from $\epsilon = 0$ to 16.4×10^{-2} and a second descending series from 10×10^{-2} to 6.56×10^{-2} . Due to the presence of fluctuations at low frequencies (see Fig.3), each measurement lasts 40 minutes (9600 periods) in order to converge the average power consumption $P_m(\epsilon)$. The results are reported on Fig. 4.

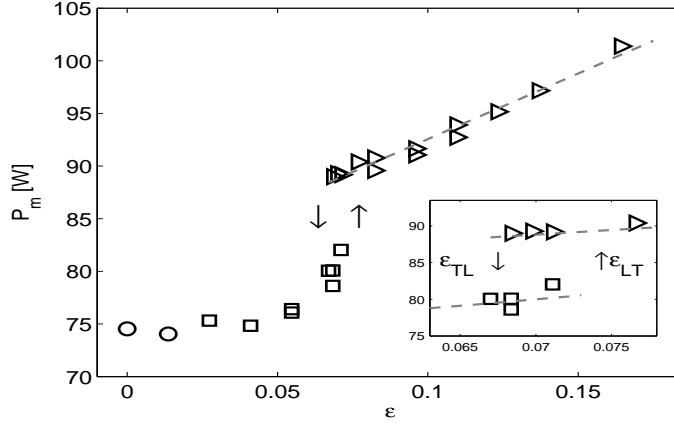


FIG. 4. Mechanical power consumption of the motor of the rotating cylinder for $\Omega_c = (8\pi)$ rad/s and $\epsilon = \Omega_t/\Omega_c \in [0, 0.165]$. Two distinct branches are clearly observable: the lower branch (L) with the laminar regime (circle) and the non-linear regimes (square), and the turbulent branch (T) (triangle). Dashed line: linear fit with $P_m = P_{m0} + C\epsilon$. Insert: zoom on the hysteresis. The system jumps from the L branch to the T branch at $\epsilon_{LT} = (7.3 \pm 0.1) \times 10^{-2}$ and goes back from T to L at $\epsilon_{TL} = (6.7 \pm 0.1) \times 10^{-2}$.

The average power consumption $P_m(\epsilon)$ displays two distinct branches: the lower branch L (squares and circles) with $\epsilon \in [0, \epsilon_{LT}]$ and the turbulent branch T (triangles) with $\epsilon \in [\epsilon_{TL}, 16 \times 10^{-2}]$. The L branch corresponds to the laminar regime (circle) and to the non-linear regime (square). Both branches are disconnected and the system undergoes a subcritical bifurcation from L to T at ϵ_{LT} and goes back from T to L at ϵ_{TL} . The thresholds are $\epsilon_{LT} = 7.3 \pm 0.1 \times 10^{-2}$ and $\epsilon_{TL} = 6.7 \pm 0.1 \times 10^{-2}$ and the hysteresis is clearly visible with $\epsilon_{LT} - \epsilon_{TL} \simeq 6 \times 10^{-3}$ (insert, Fig.4). The determination of ϵ_{LT} is very robust (section IV B) whereas a precise measurement of ϵ_{TL} is very difficult (section V A).

The behaviour of the power consumption of the L and T branches are quite different. On the L branch, the power consumption does not vary significantly for $\epsilon < 0.05$ and increases rapidly between $\epsilon \simeq 0.05$ and ϵ_{LT} . In this range, the resonant triads disappear (section III). The power consumption on the T branch exhibits a linear growth (dashed grey line on Fig.4) with

$$P_m(\epsilon) = P_0 + C\epsilon \quad (3)$$

with $P_0 = 80W$ and $C = 124W$. A similar behaviour was observed in the torque measurement of Gans²² for the hydrodynamic case.

We performed another series of measurements with constant $\epsilon = 8.75 \times 10^{-2}$ in order to estimate the Reynolds dependence of the power consumption by varying Ω_c . The flow remains turbulent for the associated Reynolds numbers, which vary in the range $[3.5, 13] \times 10^5$. To compare the measurements, we subtract the power consumption at $\epsilon = 0$ to remove the mechanical loss (increasing like Ω_c^2) of the set-up. The power injected in the flow $\Delta P = P_m(\epsilon) - P_m(0)$ is reported on the left hand side of Fig. 5. It increases like Ω_c^3 for constant ϵ . The dimensionless power $\Delta P/P_s$, with $P_s = \rho 2\pi R^4 L \Omega_c^3$, is roughly constant for $Re \in [3.5, 13] \times 10^5$ (right Fig.5), suggesting that the dimensionless injected power becomes independent of the Reynolds number.

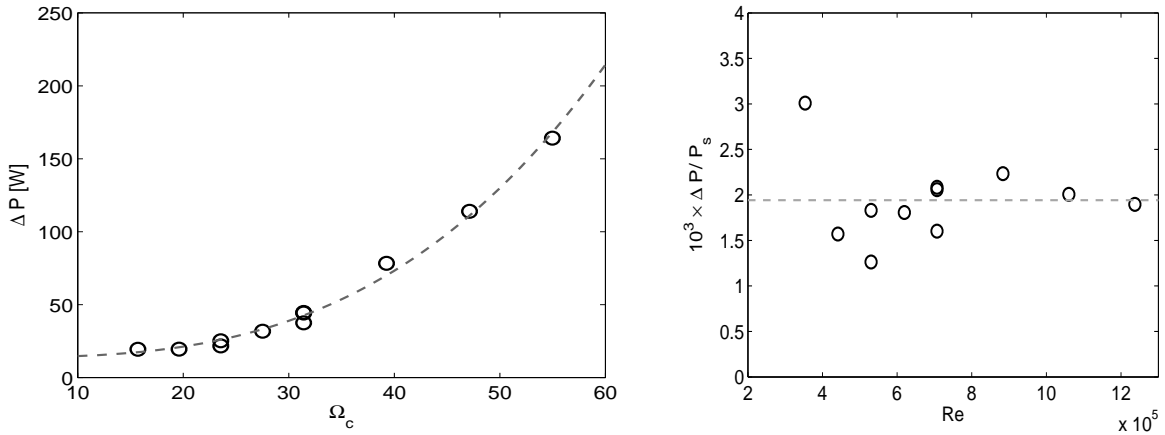


FIG. 5. Left: power injection, $\Delta P = P_m(\epsilon) - P_m(0)$ for $\epsilon = 8.7 \times 10^{-2}$ and $Re \in [3.5, 12] \times 10^5$. The dashed grey curve follows the power-law $\Delta P \sim \Omega_c^3$. Right: compensated power $\Delta P/P_s$ with $P_s = \rho 2\pi R^4 L \Omega_c^3$.

From equation 3 and the behaviour shown in Fig. 5, it can be concluded that the power dissipated into the turbulent flow scales like

$$\frac{\Delta P}{\rho R^4 L \Omega_c^3} \sim \epsilon \quad (4)$$

This scaling differs from the linear viscous theory with $\Delta P/P_s \sim \epsilon^2 Re$ and the theoretical constant bounds, $\Delta P/P_s \sim \epsilon^0$, expected for large Reynolds numbers and an infinite cylinder³⁸. Additional information about the turbulent flow is required to explain the ϵ -dependence of the above scaling law by dimensional analysis.

B. Transition to the turbulence

We have performed a series of measurements to investigate the transition to turbulence at the threshold ϵ_{LT} at a given Reynolds numbers $Re = 5.65 \times 10^5$. The precession ratio is increased step by step with a plateau time of 60 seconds ($240 f_c^{-1}$) and a precession ratio step $\Delta\epsilon = 1.42 \times 10^{-3}$. We performed 16 runs with the same procedure, using the pressure signal for the detection of the transition (see left hand side Fig.6). The transition always occurs when the precession ratio reaches the value $\epsilon = 7.25 \times 10^{-2}$. The black curve represents the precession ratio (right ordinate) and the blue curve and the red curve correspond to the pressure signal from the same probe but for two different runs. The pressure can slightly drift due to the thermal expansion of the water but we did not observe any correlation between the drift of the pressure and the onset of the instability, so we believe that this effect does not play any significant role in the dynamics of the flow. We observe at $t_d = 294s$ (resp. $t_d = 309s$) for the blue (resp. red) curve a drop of the pressure after the growth of the precession ratio to $\epsilon = 7.25 \times 10^{-2}$ at $t_p = 280s$. It corresponds to the threshold ϵ_{LT} for the transition to the turbulence. We have measured the delay $\Delta T = t_d - t_p$ between the change of ϵ and the beginning of the instability. The average value of the delay ΔT is 15 seconds ($60 f_c^{-1}$) with a standard deviation of 9 seconds ($0.6 \times \Delta T$). The delay ΔT is comparable to the precession period $f_t^{-1} = 3.3s$ and could correspond to the time needed to re-establish the base flow, which then becomes unstable. In any case, the delay ΔT is much smaller than the typical transient life time of the turbulence in the hysteresis region (see section V).

The discontinuity of the pressure confirms the presence of a subcritical transition. The

pressure jump corresponds roughly to $\Delta p \simeq 500$ Pa and is detected simultaneously on the diametrically opposed probes. The transition seems to be global and affects the low frequency components of the pressure field. The pressure drop is likely due to a slowdown of the rotation of the bulk flow. An estimation of this slowdown gives $\Delta f = (\Delta p / \rho)^{1/2} / (2\pi R) \simeq 0.7$ Hz, corresponding to 17.5% of the imposed frequency rate f_c . The slowdown of the bulk flow in the turbulent regime has also been reported for precessing cylinders²¹ and spheres³⁹.

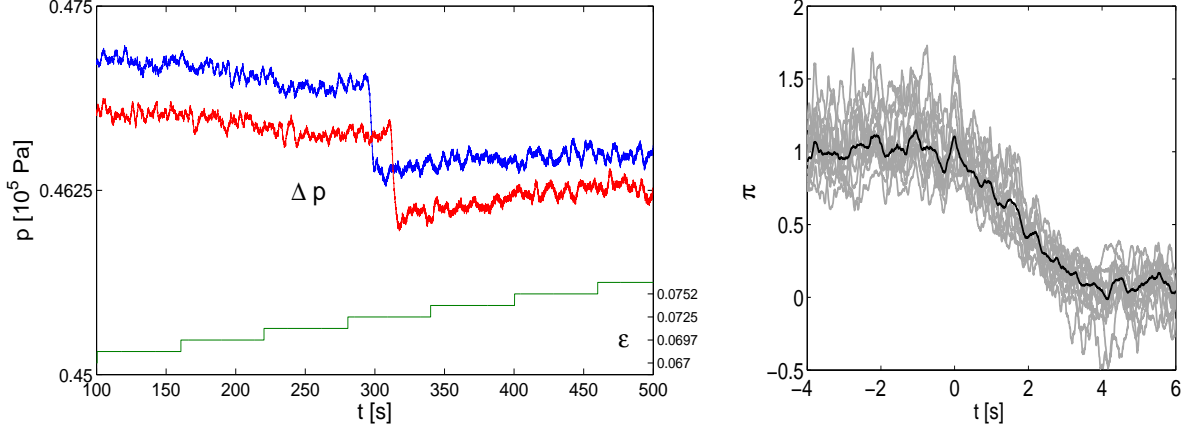


FIG. 6. Left: evolution of the low-pass filtered pressure signal p (blue and red) for two different realizations, and precession ratio ϵ (black) as a function of time t . Right: rescaled pressure π (equation 5) during the transition. The different realizations are in grey, and the averaged realization is in black.

In order to compare the different realizations, we define a rescaled pressure π such that

$$\pi(t) = \frac{p(t) - \langle p_T \rangle}{\langle p_L \rangle - \langle p_T \rangle} \quad (5)$$

with $\langle p_L \rangle$ (resp. $\langle p_T \rangle$) the average pressure before (resp. after) the transition to turbulence. The average pressure π decreases from 1 to 0. We have used a coherent average to superimpose the curves. It consists in finding the maximum of the correlation function of two different realizations, in order to remove the delay between them. The instant $t = 0$ s corresponds to the beginning of the transition. The different realizations (right hand side Fig. 6, grey curves) are concentrated around the average curve (black curve) and do not display any exponential growth or exponential relaxation to the turbulent branch. We estimate the duration of the transition $T_i = 4 \pm 0.5$ s ($16 f_c^{-1}$).

C. Effects of the Reynolds numbers

Now, we investigate the dependence of the threshold as a function of the Reynolds numbers Re . The covered parameter space (Re, ϵ) is reported on the left hand side of Fig. 7, with ϵ_{LT} (circle) and ϵ_{TL} (square). The diamonds represent the frontier between the laminar flow and the non-linear regime. It corresponds to the appearance of free Kelvin modes in the power spectrum (section III). The region between ϵ_{LT} and ϵ_{TL} corresponds to the bistable region between the L and the T branch. The threshold ϵ_{LT} depends weakly on the Reynolds number, following an empirical power law with $\epsilon_{LT} \sim Re^{-0.067}$ (Fig. 7, right). The width of the hysteresis region given by the difference $\epsilon_{LT} - \epsilon_{TL}$, is roughly independent of Re .

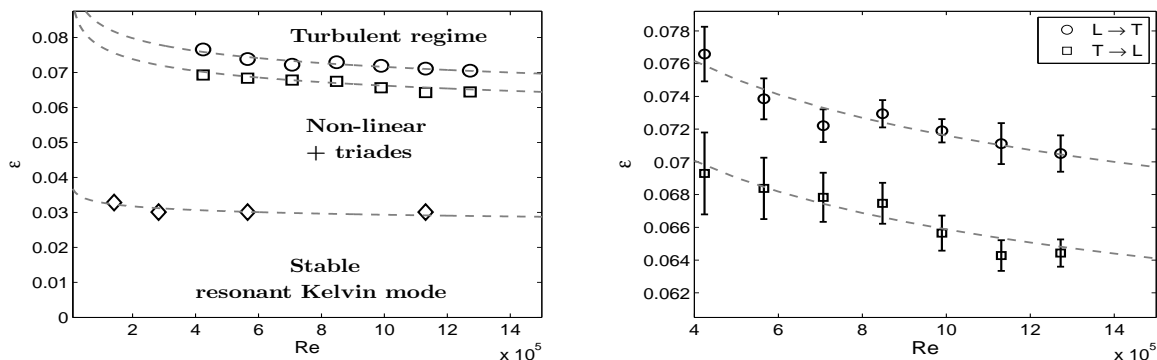


FIG. 7. Left : parameters space Re versus the measured thresholds of the first instability of the forced Kelvin mode (diamonds), the threshold ϵ_{LT} of the transition from L branch to T branch (circles) and ϵ_{TL} from T to L (squares). Right : zoom on the behaviour of ϵ_{LT} and ϵ_{TL} . Dashed curves show a fit to a power law with $\epsilon \sim Re^{-0.067}$.

V. FINITE LIFE TIME OF TURBULENCE

A. Metastability

The turbulent flow exhibits an interesting feature on the range of the hysteresis $\epsilon \in [\epsilon_{TL}, \epsilon_{LT}]$. It can suddenly cease and relax to the L branch, with a random lifetime in the turbulent branch. Figure 8 illustrates this phenomenon. The time series of the power consumption for three different runs at $Re = 5.65 \times 10^5$ are displayed on the left hand

side. For $t < 0$ s, the flow is turbulent with $\epsilon = 9.3 \times 10^{-2}$ ($> \epsilon_{LT}$) and at $t = 0$ s, the rotation rate of the turntable is reduced to $\epsilon = 6.84 \times 10^{-2}$ with $\epsilon_{TL} < \epsilon < \epsilon_{LT}$. The drop of power consumption corresponds to the transition from the T branch to the L branch. It occurs rapidly after the slowdown for the red curve, or 400s ($1.6 \times 10^3 f_c^{-1}$) for the blue curve. The third realization (black curve) is still turbulent at $t = 700$ s ($2.8 \times 10^3 f_c^{-1}$). Unlike the resonant collapse^{8,19}, the relaxation to the L branch is definitive. We did not observe spontaneous transition from the non-linear regime to the turbulent regime below the threshold ϵ_{LT} .

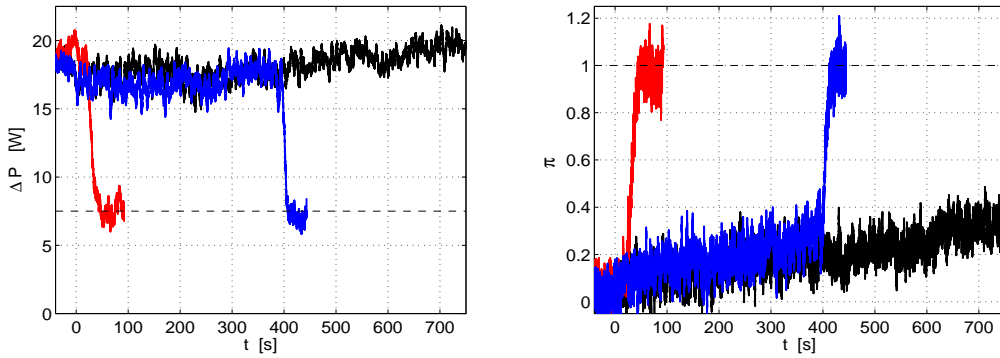


FIG. 8. Three different realizations (red, blue, black curves) of the relaxation from the T to L branches for $Re = 5.65 \times 10^5$ and $\epsilon = 8.5 \times 10^{-2}$ ($> \epsilon_{LT}$) for $t < 0$ s and $\epsilon = 6.84 \times 10^{-2}$ ($< \epsilon_{LT}$) for $t > 0$ s. Left: $\Delta P(t)$ power consumption. Right: rescaled pressure $\pi(t)$.

The pressure measurements display also an abrupt transition when the turbulence collapses. The corresponding data are reported on the right side of Fig. 8. The rescaled pressure (defined in section IV B) suddenly increases at the transition. The dynamics of this relaxation is discussed in section V C. The turbulence seems to be metastable for a given ϵ in the hysteresis region $[\epsilon_{TL}, \epsilon_{LT}]$. The lifetimes of the turbulence are random and a statistical study of the lifetimes is performed in the next section.

As mentioned in the section IV, the precise determination of ϵ_{TL} becomes intractable due to the apparent metastability of the hysteresis part of the turbulent branch. We carried out measurements for $\epsilon = 6 \times 10^{-2}$, i.e. below ϵ_{TL} , with $(\epsilon - \epsilon_{TL})/\epsilon_{TL} \simeq 10\%$. The transition is almost immediate. The delay lasts 10 s ($40 f_c^{-1}$) with a small standard deviation of 1.5 s. This time scale is comparable to the delay ΔT before the beginning of the transition

to turbulence (section IV B). It turns out that the turbulence is no more metastable for ϵ smaller than ϵ_{TL} .

B. Lifetime statistics

1. Lifetime distribution

To quantify this stochastic process, we have investigated the statistical properties of the duration of the turbulence in the metastable regime. The experimental procedure consists in starting a run at a precession ratio $\epsilon = 9.3 \times 10^{-2}$ ($> \epsilon_{LT} = 7.25 \times 10^{-2}$) in order to obtain a strong turbulent flow. After 200s ($8 \times 10^2 f_c^{-1}$), the rotation rate of the turntable is reduced to the ϵ wanted. The lifetime τ is defined as the duration between the end of the slowdown and the pressure rise, corresponding to the relaxation to the L branch (see fig 8). The incertitude concerning the end of the slowdown is of order ΔT (cf. IV).

We have performed a large number of measurements ($N = 125$) for $\epsilon = 6.7 \times 10^{-2}$ in order to calculate the probability distribution function $\rho(\tau)$ (left Fig. 9). The distribution displays an exponential tail with $\rho(\tau) \sim \exp(-\tau/\tau_0)$ and $\tau_0 = 288 \pm 30$ s or 1.1×10^3 rotation rate periods (left Fig. 9), which is characteristic of a memoryless process. The value τ_0 is close to the average lifetime $\langle \tau \rangle = 267$ s, directly calculated from the set of durations τ .

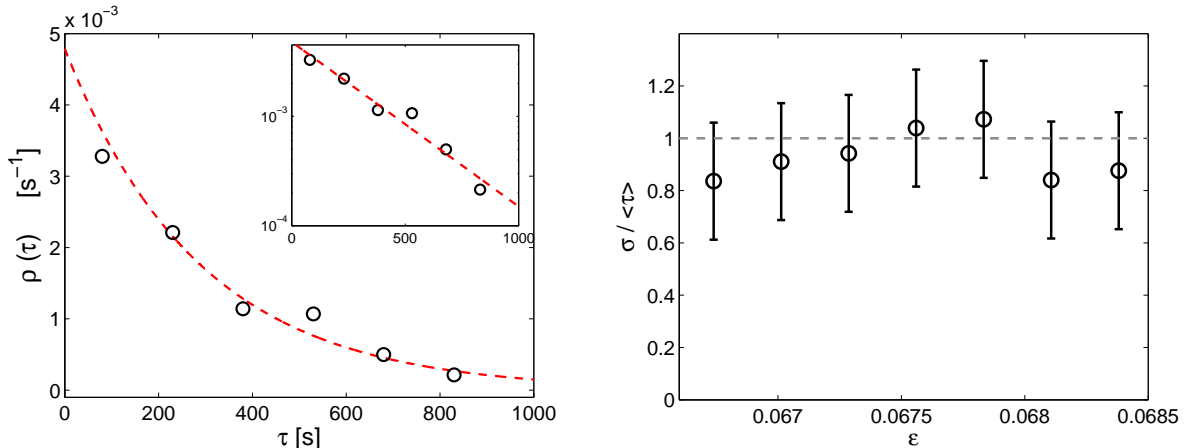


FIG. 9. Left: distribution function of the lifetime of the turbulence for $\epsilon = 6.7 \times 10^{-2}$ and $Re = 5.65 \times 10^5$ with $P(\tau) = C \exp(-\tau/\tau_0)$ with $\tau_0 = 288 \pm 30$ s. Each point corresponds to an interval of 150 s. Right: ratio of the standard deviation σ_τ over the average $\langle \tau \rangle$.

2. Average lifetime

We have performed a series of measurements to calculate the average lifetime in the turbulent branch for ϵ between 6.67×10^{-2} and 6.84×10^{-2} (Fig. 10). The average is calculated for at least 30 – 40 realizations for each precession ratio. The average lifetime $\langle \tau \rangle$ varies from 170 to 2110 seconds. It exhibits a steep increase when ϵ comes closer to ϵ_{LT} .

By assuming that $\langle \tau \rangle$ becomes infinite when ϵ is equal to ϵ_{LT} , it is tempting to model the behaviour of the average lifetime $\langle \tau \rangle$ by a critical behaviour with $\langle \tau \rangle_{th} \sim |\epsilon - \epsilon_{LT}|^{-\beta}$. Here, the critical point is "a priori" defined as equal to ϵ_{LT} but it cannot be ruled out that the critical point differs from this value. The exponent β estimated from such a fit turns out to be larger than 10, suggesting that the divergence of $\langle \tau \rangle$ is stronger than a power law. The behaviour of $\langle \tau \rangle$ is better approximated by an exponential growth with

$$\langle \tau \rangle_{th} = \exp(a|\epsilon - \epsilon_{LT}|^{-\beta} + b) \quad (6)$$

and $(a, b, \beta) = (1.08, -9.13, 1/2)$. The fit is represented by a red curve on the left hand side of Fig. 10. Equation (6) is similar to the Arrhenius equation and may refer to a behaviour called "supertransient"^{40,41} in dynamical systems.

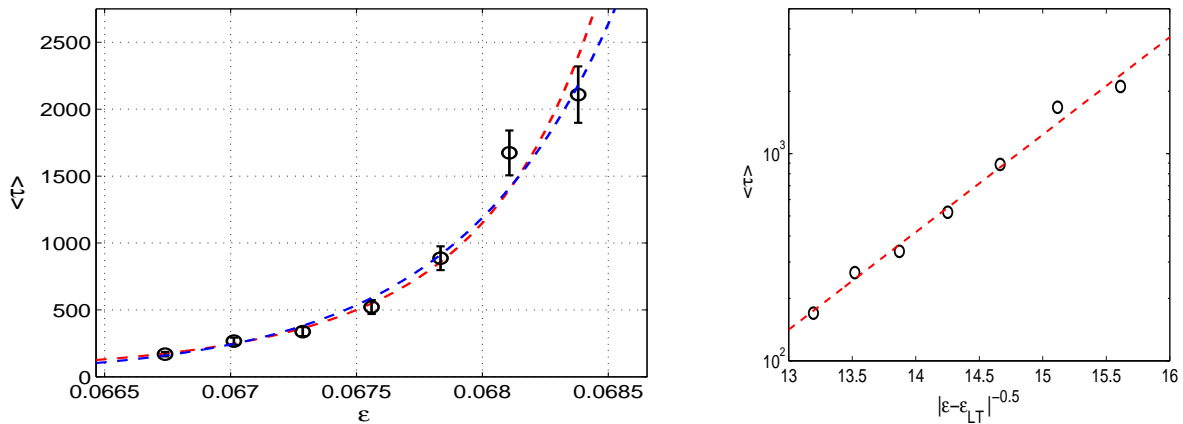


FIG. 10. Left: Average lifetime of the transient turbulence for $Re = 5.65 \times 10^5$ for different $\epsilon < \epsilon_{LT}$ ($\epsilon_{LT} = 7.3 \times 10^{-2}$). The red curve represents the functional form $\langle \tau \rangle_{th} = \exp(a|\epsilon - \epsilon_{LT}|^{-\beta} + b)$ and the blue curve corresponds to the exponential function $\langle \tau \rangle_{th} = \exp(a\epsilon + b)$. Right: Average lifetime $\langle \tau \rangle$ in function of $|\epsilon - \epsilon_{LT}|^{-0.5}$.

We have represented the escape rate $\langle\tau\rangle$ as a function of $|\epsilon - \epsilon_{LT}|^{-0.5}$ in a logarithm scale for the ordinate (right Fig.10). The circles are aligned along the red line, justifying the functional form chosen. The coefficients a and b have been estimated from the linear relation $\log(\langle\tau\rangle) = a|\epsilon - \epsilon_{LT}|^{-0.5} + b$ with a least square method, which gives a smaller relative error (cf. equation 7).

Actually, the value β can be varied in the range $[0.1, 0.7]$ without changing significantly the quality of the fit. We define the relative error function r_e as

$$r_e = \left(\frac{1}{N} \sum \frac{(\langle\tau\rangle - \langle\tau\rangle_{th})^2}{\langle\tau\rangle_{th}^2} \right)^{\frac{1}{2}} \quad (7)$$

with $N = 7$ the number of experimental points. The relative error r_e is between 9.45% and 9.55% for $\beta \in [0.1, 0.7]$ and all the functions $\langle\tau\rangle_{th}$ collapse almost on the same curve. The main contribution to the relative error r comes from the mean durations $\langle\tau\rangle$ at ϵ larger than 6.8×10^{-2} . In order to calculate more precisely the exponent β , measurements at larger ϵ , i.e. with much larger $\langle\tau\rangle$, would be needed. The quality of the fit depends also on the value of the critical point, here defined "a priori" as ϵ_{LT} .

We point out that the behaviour of $\langle\tau\rangle$ can be also approximated by an exponential function with $\langle\tau\rangle_{th} \sim \exp(a\epsilon)$ with a relative error $r_e = 7\%$ (Right Fig.10, blue dashed line). The fit is even better than with the equation 6, but it implies that the turbulence remains always metastable.

The difference between the relative error of the exponential law and the equation 6 comes from the contribution of the two last points, where the incertitude on the measured $\langle\tau\rangle$ is large (around 10%). It implies that our limited set of measurements does not allow us to decide if there is a threshold (cf equation 6) or if the turbulence remains metastable for larger ϵ (exponential law). An estimation of $\langle\tau\rangle$ for ϵ_{LT} with the exponential law gives $\langle\tau\rangle = 10^6$ s or 11 days. It implies that the experimental investigation of $\langle\tau\rangle$ near ϵ_{LT} is impossible with our set-up.

With the same set of measurements, we have calculated the standard deviation of $\langle\tau\rangle$ for different ϵ . The standard deviation σ_τ normalized by $\langle\tau\rangle$ (right Fig.9) is close to one, as expected for an exponential distribution.

C. Relaxation process

The relaxation from the turbulent to the lower branch is a fast process, compared to the transient lifetime of turbulence. We noticed by direct visualization that the turbulent flow still fills the entire vessel (like in the right hand side of Fig.2) before the collapse of the turbulence. We have reported different realizations (in grey) of the relaxation of the pressure π on the left of Fig. 11 for $Re = 5.65 \times 10^5$ and $\epsilon = 6.7 \times 10^{-2}$. The procedure is identical to the one detailed in section IV B.

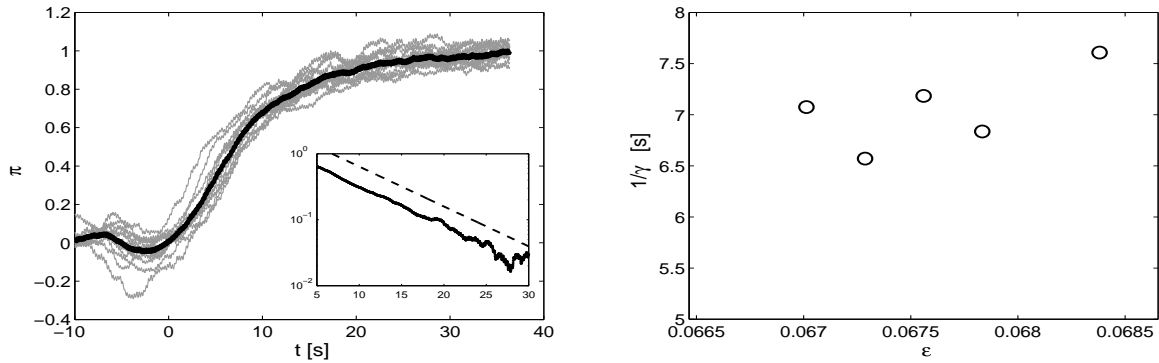


FIG. 11. Left : superposition of different realizations (in grey) of the relaxation process for $Re = 5.65 \times 10^5$ and $\epsilon = 6.7 \times 10^{-2}$ of the low-pass filtered pressure. The black curve is the average, which follows an exponential function (insert). Right: the relaxation time γ^{-1} versus the precession ratio.

All the realizations are concentrated around the average (left hand side of Fig.11, black curve). Unlike the stochastic process of the lifetimes, the relaxation seems to be deterministic with a small variability in the realizations. The transition lasts roughly 20 seconds. The end of the process ($t > 5$ s) follows an exponential relaxation with $\pi - 1 \sim \exp(-\gamma t)$ and $\gamma > 0$ (insert in left hand side Fig.11). The relaxation times γ^{-1} are reported for different ϵ on the right of Fig. 11. The parameter γ^{-1} is almost constant and stays in the range $[6.5, 7.5]$ seconds. For $\epsilon = 6 \times 10^{-2}$ ($< \epsilon_{TL}$), the relaxation remains also exponential with a similar time scale $\gamma^{-1} = 7.69$ s, even if the turbulent state is no more metastable in this range of ϵ (cf section V A).

VI. CONCLUSION

A. Summary

In the present study of a precession driven flow, we have confirmed the existence of a subcritical bifurcation to turbulence associated with a discontinuity and a hysteresis. The observed transition to turbulence is a robust process and occurs above a well defined threshold ϵ_{LT} , different from the one of the parametric instability of the forced Kelvin mode. Both the pressure and power consumption measurements exhibit an abrupt variation at the transition from and to turbulence. The behaviour of the power consumption changes at the threshold, with a linear dependence of the power on the precession ratio. The pressure measurements suggest that the transition is associated with a slowdown of the solid body rotation. The threshold ϵ_{LT} of the transition depends weakly on the Reynolds numbers.

In the region of the hysteresis $\epsilon \in [\epsilon_{TL}, \epsilon_{LT}]$, the turbulence can suddenly collapse and lead to a definitive relaminarization of the flow. For a given precession ratio and Reynolds number, the lifetimes τ of the turbulence are random and are exponentially distributed. The average lifetimes $\langle \tau \rangle$ of the turbulence increase rapidly when ϵ approaches the threshold ϵ_{LT} of the sustained turbulence. The growth of the lifetimes τ is well modelled either by the functional form $\langle \tau \rangle \sim \exp(a|\epsilon - \epsilon_{LT}|^{-\beta})$ with a and β positive or an exponential law. A detailed study of the relaxation process shows that the slow component of the pressure follows an exponential function with a relaxation rate weakly dependent of ϵ , even for $\epsilon < \epsilon_{TL}$.

As a conclusion, a schematic bifurcation diagram is presented on the Fig. 12. Three regimes are observed : the laminar and the non-linear regimes on the L branch and the turbulent regime on the T branch (cf section III). The L branch becomes unstable at ϵ_{LT} and the system undergoes a subcritical bifurcation to turbulence. The flow comes back to the L branch for ϵ smaller than ϵ_{TL} (cf section IV). Between ϵ_{TL} and ϵ_{LT} , the turbulent regime is metastable and exhibits transient lifetimes (cf section V). The sneaking arrow corresponds to the relaxation process to the lower branch. The grey line represents the frontier between the basins of attraction of each branch, even if the turbulence is not strictly speaking an attractor. The collisions between the grey and blue lines (black dots) are only symbolic and do not refer to a saddle-node bifurcation.

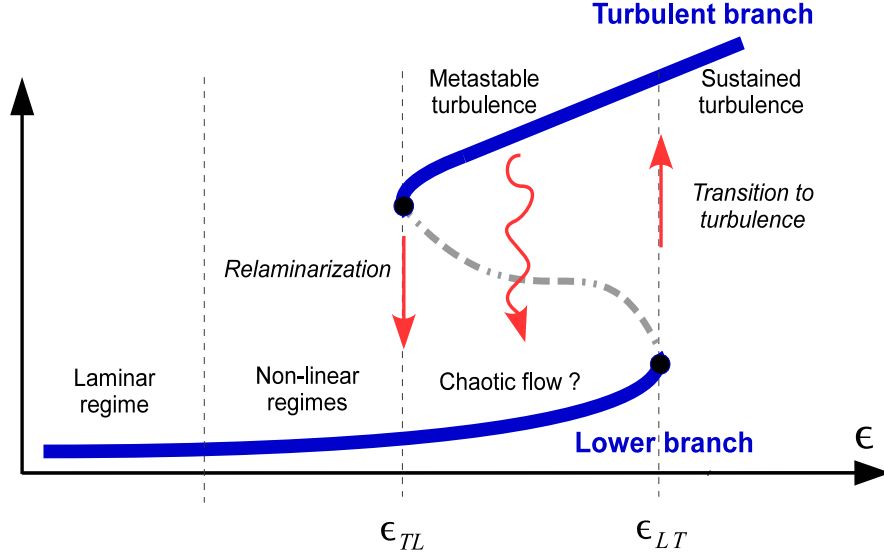


FIG. 12. Schematic bifurcation diagram of the precessing cylinder for $\epsilon < 16 \times 10^{-2}$ and $Re \in [10^5, 10^6]$.

B. Discussion

The observation of a well-defined threshold ϵ_{LT} for a sustained turbulence may lead to different conclusions. It could indicate the presence of a linear instability past the onset ϵ_{LT} . The instability could also be triggered by non-normal and non-linear mechanisms. Moreover, if we consider the flow as already chaotic before the instability, the transition could be explained by a crisis⁴² of this chaotic set. This bifurcation refers to the collision of the basin of attraction of two chaotic attractors, leading to the emergence of only one attractor. However, a non-linear instability is not consistent with the measured robustness of the threshold, whereas the crisis would be associated with random waiting times before the transition. The linear instability is thus the best candidate for the transition to turbulence. As the instability of the laminar flow occurs for smaller precession ratios than ϵ_{LT} , the mechanism of this new instability could differ from the parametric instability of the Kelvin modes¹⁶.

ACKNOWLEDGMENTS

The authors are grateful for support by the Helmholtz Allianz LIMTECH and kindly acknowledge discussions with T. Weier, B. Wustmann, T. Albrecht, C. Nore, J. Léorat, A. Tilgner and J. Noir.

REFERENCES

- ¹M. Le Bars, D. Cébron, and P. Le Gal, “Flows driven by libration, precession, and tides,” *Ann. Rev. Fluid Mech.* **47**, 260–268 (2014).
- ²W. Malkus, “Precession of the earth as the cause of geomagnetism experiments lend support to the proposal that precessional torques drive the earth’s dynamo,” *Science* **160**, 259–264 (1968).
- ³A. Tilgner, “Precession driven dynamos,” *Phys. of Fluids* **17**, 034104 (2005).
- ⁴C. Nore, J. Léorat, J.-L. Guermond, and F. Luddens, “Nonlinear dynamo action in a precessing cylindrical container,” *Phys. Rev. E* **84**, 016317 (2011).
- ⁵F. Stefani, S. Eckert, G. Gerbeth, A. Giesecke, T. Gundrum, C. Steglich, T. Weier, and B. Wustmann, “Dresdyn- a new facility for mhd experiments with liquid sodium,” *Magnetohydrodynamics* **48**, 103–113 (2012).
- ⁶F. Stefani, T. Albrecht, G. Gerbeth, A. Giesecke, T. Gundrum, J. Herault, C. Nore, and C. Steglich, “Towards a precession driven dynamo experiment,” *Magnetohydrodynamics* **51**, 275–284 (2015).
- ⁷A. Giesecke, T. Albrecht, G. Gerbeth, T. Gundrum, and F. Stefani, “Numerical simulations for the dresdyn precession dynamo,” *Magnetohydrodynamics* **51**, 293–302 (2015).
- ⁸A. McEwan, “Inertial oscillations in a rotating fluid cylinder,” *J. Fluid Mech.* **40**, 603–640 (1970).
- ⁹R. Manasseh, “Distortions of inertia waves in a rotating fluid cylinder forced near its fundamental mode resonance,” *J. Fluid Mech.* **265**, 345–370 (1994).
- ¹⁰J. J. Kobine, “Inertial wave dynamics in a rotating and precessing cylinder,” *J. Fluid Mech.* **303**, 233–252 (1995).
- ¹¹P. Meunier, C. Eloy, R. Lagrange, and F. Nadal, “A rotating fluid cylinder subject to weak precession,” *J. Fluid Mech.* **599**, 405–440 (2008).

- ¹²X. Liao and K. Zhang, “On flow in weakly precessing cylinder: the general asymptotic solution,” *J. Fluid Mech.* **709**, 610–620 (2012).
- ¹³L. Kelvin, “Vibration of a columnar vortex,” *Phil. Mag.* **10**, 155–168 (1880).
- ¹⁴Kudlick, *On the transient motion in a contained rotating fluid, PhD thesis* (Massachusetts Institute of Technology, 1966).
- ¹⁵R. Kerswell and C. Barenghi, “On the viscous decay rates of inertial waves in a rotating circular cylinder,” *J. Fluid Mech.* **285**, 203–214 (1995).
- ¹⁶R. Kerswell, “Secondary instabilities in rapidly rotating fluids: inertial wave breakdown,” *J. Fluid Mech.* **382**, 283–306 (1999).
- ¹⁷R. Lagrange, C. Eloy, F. Nadal, and P. Meunier, “Instability of a fluid inside a precessing cylinder,” *Phys. of Fluids* **20**, 081701 (2008).
- ¹⁸R. Lagrange, P. Meunier, F. Nadal, and C. Eloy, “Precessional instability of a fluid cylinder,” *J. Fluid Mech.* **666**, 104–145 (2011).
- ¹⁹R. Manasseh, “Breakdown regimes of inertia waves in a precessing cylinder,” *J. Fluid Mech.* **243**, 261–296 (1992).
- ²⁰Y. Lin, J. Noir, and A. Jackson, “Experimental study of fluid flows in a precessing cylindrical annulus,” *Phys. of Fluids* **26**, 046604 (2014).
- ²¹W. Mouhali, T. Lehner, J. Léorat, and R. Vitry, “Evidence for a cyclonic regime in a precessing cylindrical container,” *Experiments in fluids* **53**, 1693–1700 (2012).
- ²²R. F. Gans, “On hydromagnetic precession in a cylinder,” *J. Fluid Mech.* **45**, 111–130 (1971).
- ²³P. Manneville, *Dissipative Structures and Weak Turbulence* (Academic, Boston, 1990).
- ²⁴B. Eckhardt, T. M. Schneider, B. Hof, and J. Westerweel, “Turbulence transition in pipe flow,” *Annu. Rev. Fluid Mech.* **39**, 447–468 (2007).
- ²⁵F. Daviaud, J. Hegseth, and P. Bergé, “Subcritical transition to turbulence in plane couette flow,” *Phys. Rev. Lett.* **69**, 2511 (1992).
- ²⁶O. Dauchot and F. Daviaud, “Finite amplitude perturbation and spots growth mechanism in plane couette flow,” *Phys. Fluids*. **7**, 335–345 (1995).
- ²⁷S. Bottin, F. Daviaud, P. Manneville, and O. Dauchot, “Discontinuous transition to spatiotemporal intermittency in plane couette flow,” *Europhys. Lett.* **43**, 171 (1998).
- ²⁸Y. Ponty, Y. Laval, B. Dubrulle, F. Daviaud, and J. Pinton, “Subcritical dynamo bifurcation in the Taylor-Green flow,” *Phys. Rev. Lett.* **99**, 224501 (2007).

- ²⁹J. Herault, F. Rincon, C. Cossu, G. Lesur, G. Ogilvie, and P.-Y. Longaretti, “Periodic magnetorotational dynamo action as a prototype of non-linear magnetic-field generation in shear flows,” *Phys. Rev. E* **84**, 036321 (2011).
- ³⁰A. Riols, F. Rincon, C. Cossu, G. Lesur, Ogilvie, P.-Y. Longaretti, and J. Herault, “Global bifurcations to subcritical magnetorotational dynamo action in keplerian shear flow,” *J. Fluid Mech.* **731**, 1–45 (2013).
- ³¹S. Grossmann, “The onset of shear flow turbulence,” *Rev. mod. phys.* **72**, 603 (2000).
- ³²B. Hof, J. Westerweel, T. M. Schneider, and B. Eckhardt, “Finite lifetime of turbulence in shear flows,” *Nature* **443**, 59–62 (2006).
- ³³S. Bottin and H. Chaté, “Statistical analysis of the transition to turbulence in plane couette flow,” *Eur. Phys. J. B* **6**, 143–155 (1998).
- ³⁴D. Borrero-Echeverry, M. F. Schatz, and R. Tagg, “Transient turbulence in taylor-couette flow,” *Phys. Rev.E* **81**, 025301 (2010).
- ³⁵E. L. Rempel, G. Lesur, and M. R. Proctor, “Supertransient magnetohydrodynamic turbulence in keplerian shear flows,” *Phys. Rev. Lett.* **105**, 044501 (2010).
- ³⁶I. Grants and G. Gerbeth, “Experimental study of non-normal nonlinear transition to turbulence in a rotating magnetic field driven flow,” *Phys. of Fluids* **15**, 2803–2809 (2003).
- ³⁷H. Greenspan, *The theory of rotating fluids*. (Cambridge Univ Press, 1969).
- ³⁸R. Kerswell, “Upper bounds on the energy dissipation in turbulent precession,” *J. Fluid Mech.* **321**, 335–370 (1996).
- ³⁹S. Goto, N. Ishii, S. Kida, and M. Nishioka, “Turbulence generator using a precessing sphere,” *Phys. of Fluids* **19**, 061705 (2007).
- ⁴⁰C. Grebogi, E. Ott, and J. A. Yorke, “Super persistent chaotic transients,” *Ergodic Theory and Dynamical Systems* **5**, 341–372 (1985).
- ⁴¹T. Tél and Y.-C. Lai, “Chaotic transients in spatially extended systems,” *Phys. Reports* **460**, 245–275 (2008).
- ⁴²C. Grebogi, E. Ott, and J. A. Yorke, “Chaotic attractors in crisis,” *Phys. Rev. Lett.* **48**, 1507 (1982).